J. Fluid Mech. (2014), *vol.* 738, *pp.* 250–267.
doi:10.1017/jfm.2013.597

Scaling the propulsive performance of heaving flexible panels

Daniel B. Quinn[1,†], **George V. Lauder**[2] **and Alexander J. Smits**[1,3]

[1]Department of Mechanical and Aerospace Engineering, Princeton University, Princeton, NJ 08544, USA
[2]Department of Organismic and Evolutionary Biology, Harvard University, Cambridge, MA 02138, USA
[3]Department of Mechanical and Aerospace Engineering, Monash University, Victoria, Australia

(Received 22 August 2013; revised 30 October 2013; accepted 5 November 2013)

We present an experimental investigation of flexible panels actuated with heave oscillations at their leading edge. Results are presented from kinematic video analysis, particle image velocimetry, and direct force measurements. Both the trailing edge amplitude and the mode shapes of the panel are found to scale with dimensionless parameters originating from the Euler–Bernoulli beam equation. The time-averaged net thrust increases with heaving frequency, but experiences localized boosts near resonant frequencies where the trailing edge amplitude is maximized. These boosts correspond to local maxima in the propulsive efficiency. For a constant heave amplitude, the time-averaged net thrust coefficient is shown to be a function of Strouhal number over a wide range of conditions. It appears, therefore, that self-propelled swimming (zero net thrust) only occurs over a small range of Strouhal numbers. Under these near-constant Strouhal number conditions, the propulsive economy increases with higher flexibilities and slower swimming speeds.

Key words: flow–structure interactions, propulsion, swimming/flying

1. Introduction

Flexibility is one of the defining characteristics of fish propulsion, where fine musculature and compliant membranes allow both active and passive control of fin kinematics (Lauder & Madden 2007). Moreover, flexibility allows complex kinematics to result from rather simple forcing patterns, an effect with important consequences for swimming efficiency (Bhalla, Griffith & Patankar 2013). These observations have led to a considerable body of literature concerning the role of flexibility in propulsive performance. Interest can be dated to the work of Wu (1971), who showed analytically that slender flexible bodies could achieve higher efficiencies than their rigid counterparts. Katz & Weihs (1978) both verified these predictions and extended them to large amplitude motions using an inviscid panel method.

More recently, advances in biologically inspired underwater vehicles have led to new-found interest in flexible propulsors: see, for example, Low (2011) or Lauder *et al.* (2011). Specifically, chordwise flexibility has been shown to increase propulsive efficiency in experiments (Prempraneerach, Hover & Triantafyllou 2003) and direct

† Email address for correspondence: danielq@princeton.edu

numerical simulations (Pederzani & Haj-Hariri 2006; Zhu 2007). In the past few years, much attention has been given to the resonant frequency of the propulsor, and most studies report the highest efficiencies occurring when the actuation frequency f is within 10 % of the first resonant frequency $\hat{f}_1$. This finding has held true in a variety of experiments (Heathcote & Gursul 2007; Spagnolie *et al.* 2010; Leftwich *et al.* 2012; Dewey *et al.* 2013) and numerical studies (Michelin & Llewellyn Smith 2009; Paulo, Ferreira de Sousa & Allen 2011).

In contrast, several studies in the micro-aerial vehicle (MAV) literature have found efficiencies to be maximized for f considerably lower than $\hat{f}_1$. Through experiments (Ramananarivo, Godoy-Diana & Thiria 2011), direct numerical simulations (Vanella *et al.* 2009), and order-of-magnitude scaling arguments (Kang *et al.* 2011), the optimum f was found to be as low as 33–50 % of $\hat{f}_1$. In these MAV studies, the surrounding air is much less dense than the propulsor itself, and the differences are presumed to be due to the relative importance of the inertia of the propulsor; for a thorough discussion see Daniel & Combes (2002) or Kang *et al.* (2011).

To examine the effects of flexibility and to identify scaling relationships, we are motivated to investigate flexible propulsors with simple geometries and actuations. A similar strategy was adopted by Dewey *et al.* (2013), who studied the thrust production of rectangular flexible panels undergoing pitch oscillations at the leading edge. The current study advances this work in three directions. First, we investigate multiple flow speeds, so that we can change the Strouhal number (the non-dimensional flapping frequency) by varying the frequency and/or the flow speed. By changing the flow speed, we can also investigate multiple 'self-propelled' swimming conditions, that is, cases in which the panels experience zero net thrust. Second, the wide range of flexibilities and longer chord used here allow excitation of the first four modes of flapping, whereas only the first mode was considered by Dewey *et al.* (2013). We will therefore be able to demonstrate that linear beam theory is applicable to swimming kinematics up to the fourth resonant mode. Finally, the oscillations are in heave, not pitch, but we will show that the relevant scaling parameters will be similar in form.

In this respect, the work of Alben *et al.* (2012), who studied the swimming speeds of flexible rectangular panels actuated with heaving oscillations at the leading edge, is directly relevant to the current study. All cases considered were self-propelled, which differs from the current study, where both negative and positive net thrust conditions are considered. Their inviscid numerical model predicted multiple peaks in self-propelled swimming speed as the panel length and flexibility were varied. In comparison, the current study shows multiple peaks in propulsive efficiency as flexibility is varied. Finally, we will borrow analysis techniques from Allen & Smits (2001), who studied the passive motions of flexible membranes behind a bluff body. While their membranes were not directly actuated, the boundary conditions were similar, and we expect similar modal decompositions of the kinematics.

2. Experimental methods

Experiments were conducted on rectangular panels suspended in a recirculating water channel. The four panels tested had bending stiffnesses ranging from $EI = 6.9 \times 10^{-5}$ to 3.2×10^{-1} N m^2 (see table 1), where $EI = Es\delta^3/(12(1-\nu^2))$, with elastic modulus E, panel thickness δ, panel span s, and Poisson ratio ν. The Poisson ratio was estimated to be 0.3 for all panels. The moduli were measured by tensile tests of the steel (panel A) or polyethylene (panels B–D) from which the panels were made. All panels had a chord length $c = 195$ mm and a span $s = 150$ mm.

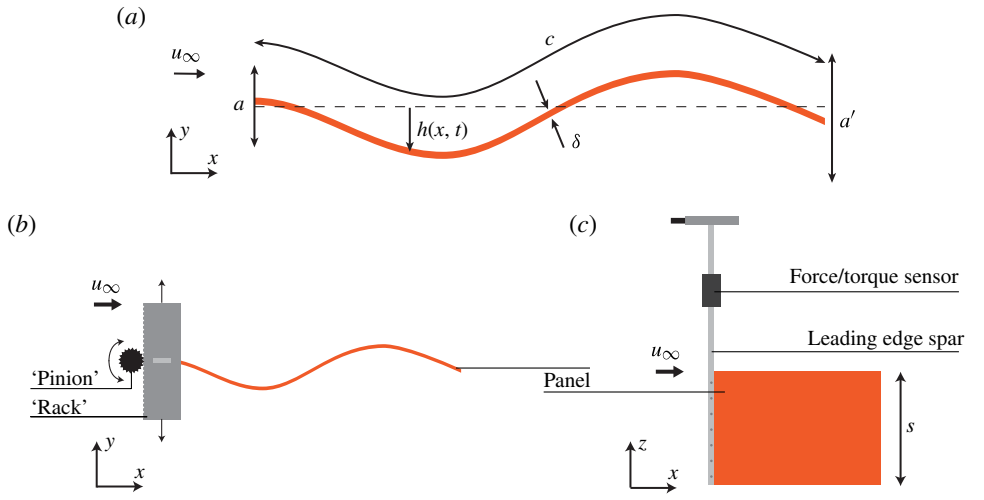

FIGURE 1. (Colour online) Experimental setup: (*a*) length scale definitions; (*b*) top view; (*c*) side view.

Panel	E (GPa)	δ (mm)	EI (N m^2)
A	82.0	0.66	3.2×10^{-1}
B	1.7	0.77	1.1×10^{-2}
C	1.8	0.32	8.1×10^{-4}
D	3.8	0.11	6.9×10^{-5}

TABLE 1. Panel specifications.

The panels were actuated at the leading edge by an aluminium spar undergoing sinusoidal heave oscillations with frequency f and peak-to-peak amplitude a (see figure 1). The 29 frequencies considered ranged from 0 to 3.5 Hz at intervals of 0.125 Hz. The leading amplitude a was 20 mm for all trials, while the trailing amplitude a' was a passive output of the system. The position of the leading edge y_{LE} was checked with an optical encoder, and it did not deviate by more than 1 % from the input waveform. The leading edge spar was connected to a rack which heaved back and forth under the action of a servo motor. Along the spar (between the mount and the panel) was a 6-axis force/torque sensor (ATI Inc., Nano-25 SI-125-3 for panels A and B, Nano-17 SI-50-0.5 for panels C and D) which was used to measure streamwise and lateral forces ($\mathcal{F}_x$ and $\mathcal{F}_y$, respectively).

The surface of the water downstream of the panel was covered with a planar baffle to reduce surface waves. With the baffle in place, surface waves were only found to be significant for panel A actuated at frequencies near the first gravity wave harmonic, which occurs at $f \approx 1.8$ Hz based on the dimensions of the channel. Left untreated, panel C experienced significant spanwise curvature. This curvature was eliminated by using two strips of aluminium shimstock to increase the spanwise rigidity.

The net streamwise force $\mathcal{F}_x$ is equal to the thrust produced by the panel minus the drag imposed by the flow. For notational convenience we will use 'net thrust' (τ) to denote 'net force in the x direction' ($\mathcal{F}_x$). The power input to the fluid is given

by $\wp = -\mathcal{F}_y v_{LE}$, where v_{LE} is the lateral velocity of the leading edge, and will simply be referred to as the 'power' ($\wp$). The instantaneous net thrust and power data were filtered using a 12 Hz LP second-order digital Butterworth filter and phase-averaged (denoted by a tilde) over the largest number of oscillation cycles possible in a 10 s period of data acquisition. Time-averages (denoted by an overbar) were taken by averaging over the same oscillation cycles. The average variance over all conditions was ± 13 mN for $\bar{T}$ and $\tilde{T}$, and ± 3 mW for $\bar{P}$ and $\tilde{P}$. These estimates were lower for panels C and D, where the higher resolution force/torque sensor reduced the average variances to ± 5 mN and ± 1 mW.

In addition to force/torque data, the kinematics of the panel were recorded by filming the edge view (seen in the x–y plane) with a high-speed camera (Photron, FASTCAM 1024 PCI). An in-house edge-tracking code identified the shape of the panel at 200 Hz. The trailing edge amplitude a' was taken to be the difference between extrema of the trailing edge position, averaged over the same cycles as were used for net thrust and power averages. At the lowest flow speed, panel D became unstable for $f \geqslant 2.75$ Hz, and a' deviated by more than 10 % between cycles. Data for these conditions will be reported but highlighted in the figures.

Using the same camera setup, particle image velocimetry (PIV) was conducted at the midspan for a sampling of cases. The laser sheet was generated by a continuous 10 W argon-ion laser (Coherent, Innova 70-C), and the particles were hollow silver-coated glass beads with an average diameter of 12 μm. Black ink was used to reduce diffuse laser reflections off the panels to a region adjacent to the panel surface with a thickness ≈ 1 mm. The velocity field was calculated using Davis 8.1.3, the spatial cross-correlation algorithm developed by LaVision Inc. (Stanislas *et al.* 2005). In total, nine passes with 50 % overlap were conducted on the data: three with 128×128 pixel windows, three with 64×64, and three final passes with 32×32. The resulting velocity field consisted of 64×64 vectors. In quadrature, the instantaneous velocity errors are estimated to be 1–5 % (Sciacchitano, Wieneke & Scarano 2013).

To summarize, the input parameters are the chord (c), span (s), and bending stiffness (EI) of the panel; the peak-to-peak amplitude (a) and frequency (f) of the heave oscillations; the density (ρ) and viscosity (μ) of water; and the speed of the incoming flow (u_∞). These eight variables yield five dimensionless parameters. The first two are geometric: the aspect ratio ($s/c \approx 0.77$) and the amplitude/chord ratio ($a/c \approx 0.1$). These parameters were held constant. The third parameter is the Strouhal number, $St \equiv fa'/u_\infty$, where a' is a function of the other variables and must be determined *a posteriori* from the video analysis. We also define a Reynolds number based on the chord, $Re_c \equiv \rho u_\infty c/\mu$, which ranges from 7800 to 46 800 in the current study. Finally, we define the effective flexibility, $\Pi_1 \equiv (\rho s f^2 c^5/EI)^{1/2}$, which is a ratio of added mass forces to internal bending forces. Figure 2 illustrates where the current study fits in with previous work in the Re_C–Π_1 plane of the phase space.

3. Results & discussion

3.1. *Kinematics*

Small deflections h of a flexible panel with constant cross-section can be modelled by the Euler–Bernoulli beam equation (Weaver, Timoshenko & Young 1990),

$$\rho_p \delta s \frac{\partial^2 h}{\partial t^2} + EI \frac{\partial^4 h}{\partial x^4} = \mathcal{F}_{ext}, \tag{3.1}$$

where ρ_p is the density of the panel and $\mathcal{F}_{ext}$ is the external force per unit length. Since $\rho_p/\rho = O(1)$ and $\delta/c \ll 1$, we expect added mass forces to dominate over the

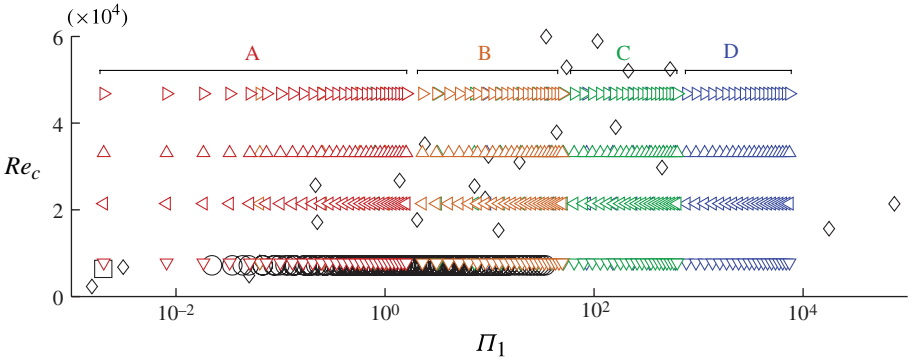

FIGURE 2. (Colour online) Parameter space. Semi-log scale. Existing propulsive panel literature: □, Buchholz & Smits (2006); ○, Dewey *et al.* (2013); ◇, Alben *et al.* (2012). Current study: ▽, $u_\infty = 40$ mm s^{-1}; ◁, $u_\infty = 110$ mm s^{-1}; △, $u_\infty = 170$ mm s^{-1}; ▷, $u_\infty = 240$ mm s^{-1}. Reynolds number $Re_C \equiv \rho u_\infty c/\mu$; effective flexibility $\Pi_1 \equiv (\rho s f^2 c^5/EI)^{1/2}$. In the online version panels A, B, C, and D are coloured red, orange, green, and blue, respectively.

inertia of the panel. We are thus motivated to replace the mass per length of the panel, $\rho_p \delta s$, with an effective mass per length, $\rho s c$. Introducing dimensionless variables $X^* \equiv x/c$, $H^* \equiv h/a'$, and $T^* \equiv tf$, the beam equation can now be written as

$$\Pi_1^2 \frac{\partial^2 H^*}{\partial T^{*2}} + \frac{\partial^4 H^*}{\partial X^{*4}} = \mathscr{F}^*_{ext}, \tag{3.2}$$

where $\mathscr{F}^*_{ext} \equiv \mathcal{F}_{ext} c^4/(EIa')$ is the dimensionless external force per unit length, except for added mass, which was incorporated into the left-hand side of the equation by introducing the effective mass per length. These additional external forces could include, for example, internal damping or viscous drag. Note the appearance of the effective flexibility, Π_1, as defined above. Since the leading edge was fixed and the trailing edge was free, the appropriate boundary conditions are $H^*(0) = 0$, $H^{*'}(0) = 0$, $H^{*''}(1) = 0$, and $H^{*'''}(1) = 0$.

The solution to (3.2) can be represented as $H^*(X^*, T^*) = \sum_{i=1}^{\infty} \xi_i(X^*)\Theta_i(T^*)$, where ξ_i are orthonormal eigenfunctions and Θ_i are the modal contributions. The eigenfunctions form a basis into which we can project the experimentally measured displacement, H^*_{exp}. The choice of basis is not unique, and here we choose the eigenfunctions for the homogeneous form of (3.2), that is, where $\mathscr{F}^*_{ext} = 0$. The advantage of this choice is that ξ_i has an exact solution with eigenvalues λ_i that follow from the boundary conditions (Weaver *et al.* 1990). The natural frequencies of these modes, $\hat{f}_i$, are such that $f/\hat{f}_i = \Pi_1 \lambda_i^2$. Hence the importance of the dimensionless variable Π_1: it is directly proportional to the ratio between the actuation and resonant frequencies when only added mass forces are modelled.

The modal contributions follow from taking an inner product of H_{exp} with each eigenfunction:

$$\Theta_i(T^*) = \int_0^1 H^*_{exp}(X^*, T^*)\xi_i(X^*)\,\mathrm{d}X^*. \tag{3.3}$$

Panels A and B exhibited only the first mode, that is, $\Theta_{i=1} \approx 1$ and $\Theta_{i\neq 1} \approx 0$ for all conditions. Panel C exhibited the first two modes, though the second mode appeared only at the lowest flow speed considered. Panel D exhibited the first four modes, and

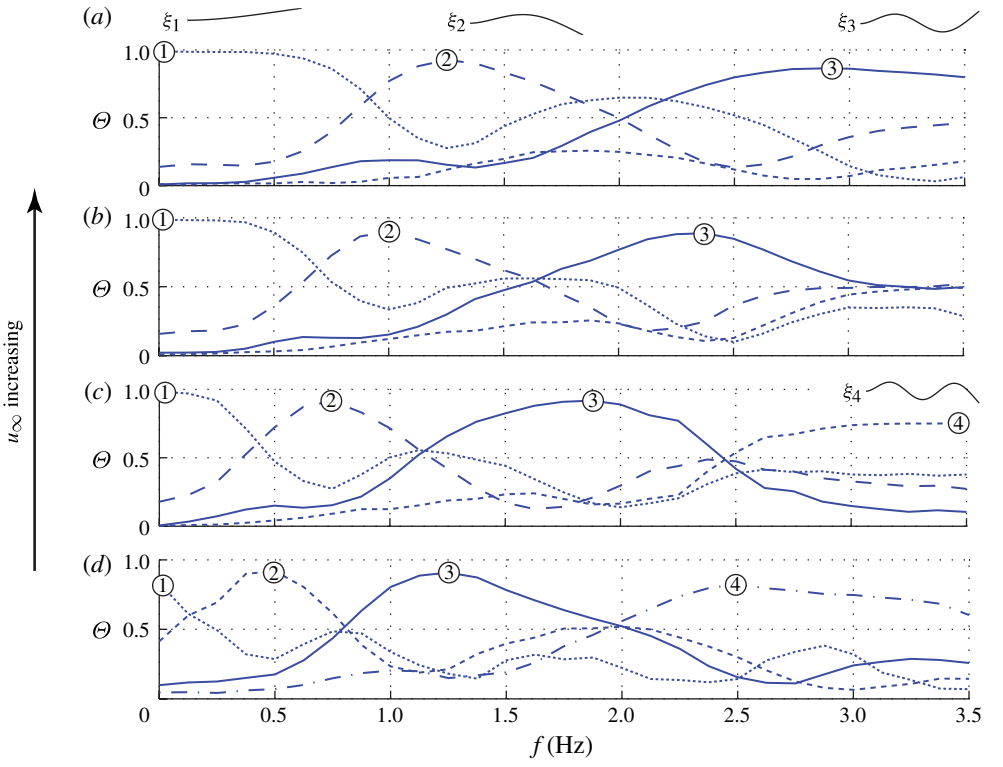

FIGURE 3. (Colour online) Mode shape projections for panel D at $T^* = 0.75$: (*a*) $u_\infty = 240$ mm s^{-1}; (*b*) $u_\infty = 170$ mm s^{-1}; (*c*) $u_\infty = 110$ mm s^{-1}; (*d*) $u_\infty = 40$ mm s^{-1}. Mode shapes: ①, mode 1; ②, mode 2; ③, mode 3; ④, mode 4 (symbols are placed at the peaks to highlight shifting modes).

provides the most insight into the structure of the modal decomposition. Figure 3 shows the modal contributions for panel D at a sample phase for each of the four flow speeds. As the heaving frequency increases, the modal contributions pass through a series of peaks as successively higher modes are actuated. As the flow speed increases, these peaks shift to higher frequencies. Heaving at 0.5 Hz, for example, actuates the second mode when $u_\infty = 40$ mm s^{-1}, but the first mode when $u_\infty = 240$ mm s^{-1}.

We now consider the trailing edge amplitude a'. At heaving frequencies where a' is locally maximized, the system is said to be operating in resonance. For each panel, the frequency at which resonance occurs is relatively independent of flow speed. Figure 4 shows that resonance occurs at four distinct values of Π_1 for all panels tested. Panel A displays the first peak, whereas the more flexible panels pass through multiple peaks over the frequency range considered. For all panels, a'/a appears to be a strong function of Π_1.

The amplitudes of the a'/a peaks show two main trends. One is a reduction in magnitude with successive peaks. The first two peaks in figure 4 show a peak-to-trough distance of $\sim$1, but this has fallen to $\sim$0.5 by the fourth peak. This behaviour is consistent with deflections being more easily suppressed by fluid forces when the panel is more flexible. The other noteworthy trend is a decrease in a'/a with increasing flow speed. Presumably the form drag at higher flow speeds suppresses panel deflections and thereby reduces the amplitude of the wave along the panel.

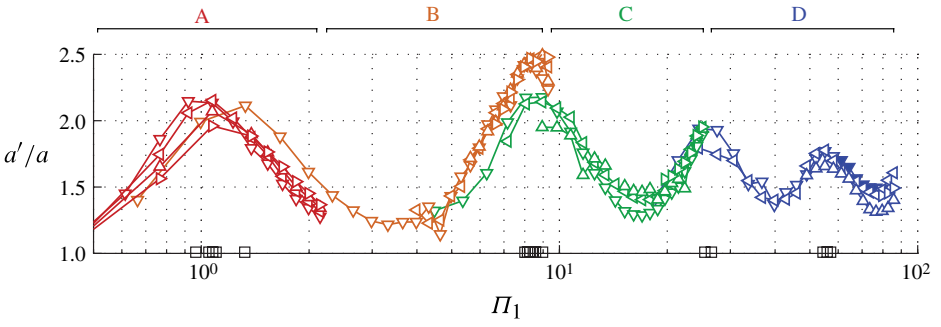

FIGURE 4. (Colour online) Trailing edge amplitude as a function of effective flexibility, $\Pi_1 \equiv (\rho s f^2 c^5/EI)^{1/2}$: $\triangledown$, $u_\infty = 40$ mm s^{-1}; $\triangleleft$, $u_\infty = 110$ mm s^{-1}; $\triangle$, $u_\infty = 170$ mm s^{-1}; $\triangleright$, $u_\infty = 240$ mm s^{-1}. Locations of a'/a peaks are highlighted along the Π_1 axis ($\square$). Filled symbols denote conditions with chaotic kinematics. Due to high scatter at low frequencies where the kinematics are heavily influenced by drag, only positive net thrust conditions ($\bar{\tau} > 0$) are plotted.

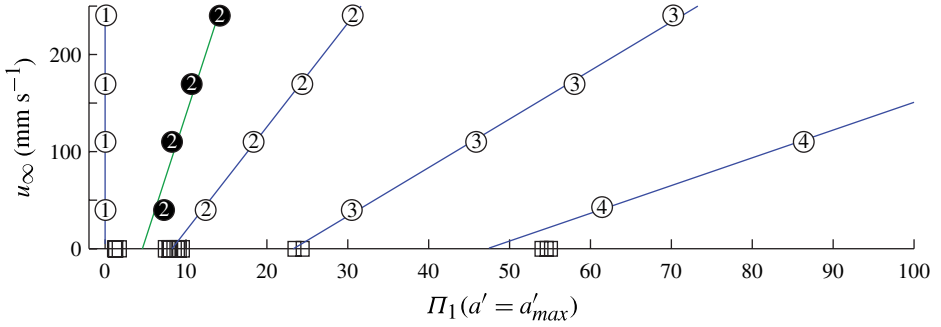

FIGURE 5. (Colour online) Mode shape symbols as in figure 3. Empty symbols, panel D; filled symbols, panel C. Solid lines are linear regressions for each mode. Locations of a'/a peaks are highlighted along the Π_1 axis ($\square$).

A linear regression of the mode peaks helps to connect the trailing edge behaviour with the modal decompositions (figure 5). The Π_1 values at which structural modes would theoretically occur when $u_\infty = 0$ coincide approximately with the Π_1 values at which a'/a is maximized (the modes could not be measured directly at $u_\infty = 0$, because with no flow to stabilize the travelling wave, the panel kinematics become chaotic). It appears that the first-order effect of form and viscous drag is to stretch the shape of the panel in the streamwise direction but leave the resonant frequencies relatively unaffected.

3.2. *Flow field*

The flow surrounding the panel is characterized by regions of concentrated vorticity along the surfaces of the panel and in the wake. Figure 6 shows the distribution of positive (anticlockwise) and negative (clockwise) vorticity at three frequencies for $u_\infty = 110$ mm s^{-1}. At the lowest frequency, boundary layers along the panel feed into wavy sheets of vorticity in the wake. The sign of the sheets corresponds to a jet flowing toward the body, and this case will be shown to produce a net drag on the

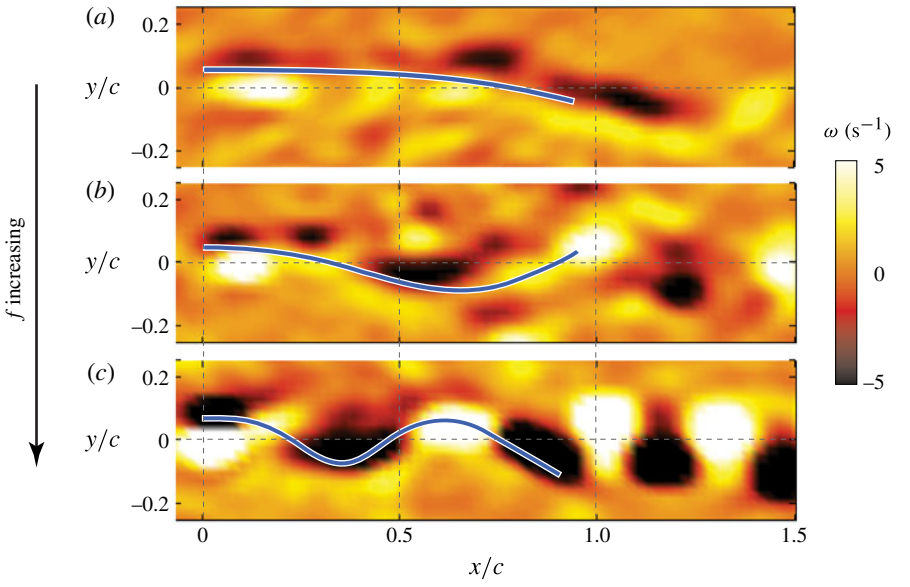

FIGURE 6. (Colour online) Frequency dependence of vorticity (ω) for panel D for $u_\infty = 110$ mm s^{-1}, at the time of maximum leading edge excursion ($\phi = 0$): (*a*) $f = 0.5$ Hz; (*b*) $f = 2.6$ Hz; (*c*) $f = 3.5$ Hz.

panel. As the frequency increases, the wake vorticity is concentrated into cores until a typical vortex street is present. In these cases, the downstream momentum flux is positive and the panel experiences net thrust.

The shape of the panel in figure 6 depicts how higher modes are excited by higher frequencies. The higher modes are also seen to produce a qualitatively different vorticity distribution along the surface of the panel. Unlike at lower frequencies, vorticity alternates along both sides of the surface of the panel, and the alternation is locked in phase with the travelling wave. We expect that in these cases the steady component of the pressure distribution will have periodicity matching that of the actuation. This will have important consequences for the instantaneous forces exerted on the panel.

Figure 7 shows the vorticity distributions at three flow speeds for $f = 2$ Hz. The spacing of the vortices increases with flow speed due to faster advection rates. The shape of the panel depicts how mode peaks are shifted to higher frequencies as the flow speed increases. While the shape is mostly the third mode when $u_\infty = 40$ mm s^{-1}, it is between the third and fourth mode when $u_\infty = 170$ mm s^{-1}. In addition, the higher flow speeds cause the flow to separate off the panel surface, presumably resulting in higher form drag. This process also disrupts the alternation of vorticity along the panel surface; at $u_\infty = 170$ m s^{-1}, the periodicity is barely discernible.

In all the vorticity distributions shown, two vortices are present at the leading edge. Only one phase is shown, but these vortices remain attached to the leading edge throughout the flapping cycle. This attachment is presumably because of the high reduced frequencies $k \equiv fc/u_\infty$ considered (2.3–9.8 in figure 7), which imply that vortex dynamics are more strongly influenced by lateral motions than by the free-stream velocity. Indeed, at the lowest k-values considered here, some of the vorticity at the leading edge rolls up and travels downstream in coherent vortices. This behaviour is consistent with MAV studies (e.g. Kang *et al.* (2013)), where k is typically less

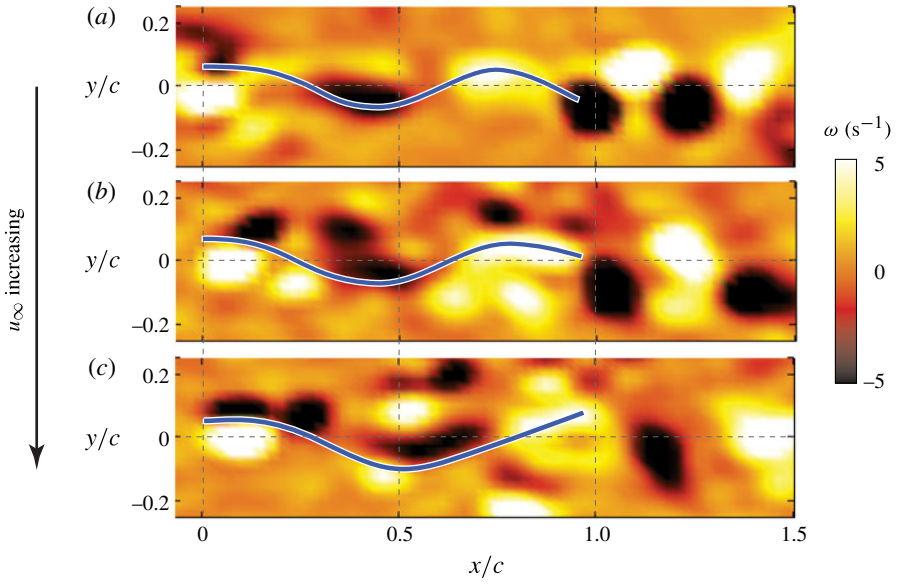

FIGURE 7. (Colour online) Flow speed dependence of vorticity (ω) for panel D for $f = 2$ Hz, at the time of maximum leading edge excursion ($\phi = 0$): (*a*) $u_\infty = 40$ mm s^{-1}; (*b*) $u_\infty = 110$ mm s^{-1}; (*c*) $u_\infty = 170$ mm s^{-1}.

than 1 and leading edge vortices are often seen to detach from the body. Under these low k conditions, the timing of leading edge vortex shedding is known to be important for propulsive efficiency (Anderson *et al.* 1998), but no such trends were observed here.

3.3. *Phase-averaged forces*

Figure 8 shows phase-averaged net thrust and power measured through the oscillation cycle at four heaving frequencies for panel D. We define ϕ as the phase of the oscillation such that ϕ ranges from 0 to 2π, with $\phi = 0$ corresponding to $y_{LE}/a = 0.5$, that is, when the leading edge is at its maximum y position. The content of the signals is dominated by a frequency of $2f$, that is, twice the heaving frequency, with peaks occurring just after the panel is in mid-upstroke ($\phi = \pi/2$) and in mid-downstroke ($\phi = 3\pi/2$). The magnitudes of both signals increase with heaving frequency, as expected. The power signal is the smoother of the two, owing to the fact that $|\mathcal{F}_y/\mathcal{F}_x| = O(c/a) \gg 1$, and thus the relative error in the power signal is expected to be much lower than the relative error in the net thrust. Unlike the net thrust signal, the power signal is negative at certain times in the oscillation cycle, specifically just after the leading edge passes through its extrema ($\phi = 0$ and $\phi = \pi$). Hence, there is a phase lag between the lateral forces and leading edge position. Just after $y_{LE}/a = 0.5$, for example, a negative power input implies that $\mathcal{F}_y$ is still negative, despite the downward motion of the panel.

Figure 9 shows the net thrust and power signals at four different flow speeds for the same panel (panel D). The frequency content and peak positions are similar to those observed in figure 8. The net thrust decreases significantly with increasing flow speed, and the reduction happens in two distinct ways. The first is an offset in the signal, causing its average to decrease and even drop below zero. The second reduction is in the magnitude of the peaks. This contribution is more likely due to the changing

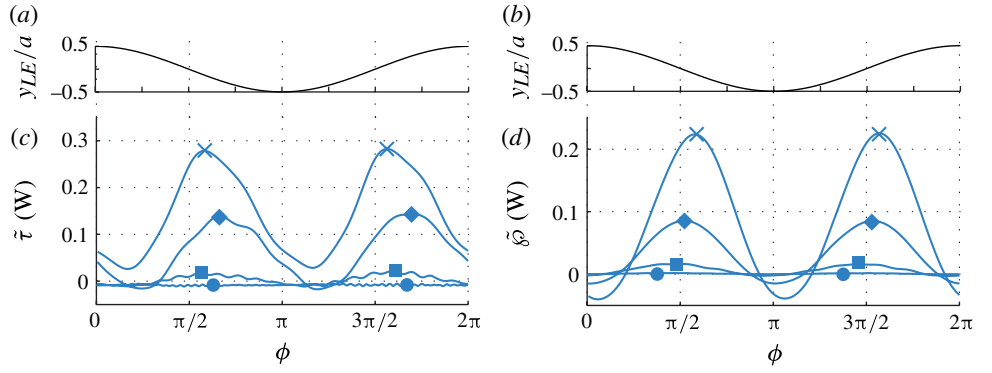

FIGURE 8. (Colour online) Frequency dependence of phase-averaged net thrust and power for panel D. (*a,b*) Position of the leading edge y_{LE}. (*c,d*) Net thrust (*c*) and power (*d*). Frequencies: ●, $f = 0.5$ Hz; ■, 1.4 Hz; ♦, 2.6 Hz; ×, 3.5 Hz.

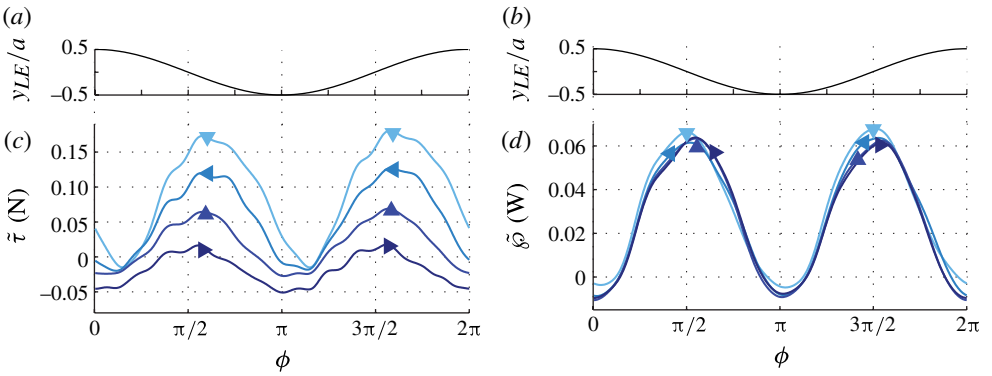

FIGURE 9. (Colour online) Flow speed dependence of phase-averaged net thrust and power for panel D. (*a,b*) Position of the leading edge y_{LE}. (*c,d*) Net thrust (*c*) and power (*d*). Flow speeds: ▼, $u_\infty = 40$ mm s^{-1}; ◄, 110 mm s^{-1}; ▲, 170 mm s^{-1}; ►, 240 mm s^{-1}.

kinematics on the panel, since the effect was less pronounced for the stiffer panels (not shown). In contrast to the net thrust, the power is unaffected by changing the flow speed, signifying that viscous effects play only a minor role in scaling the lateral forces.

We now introduce a scaling based on typical force magnitudes. We propose the following representative parameters: a fluid mass, ρsc, and the leading and trailing edge velocities, fa and fa', respectively. Following Hultmark, Leftwich & Smits (2007), who found that thrust is produced primarily at the trailing edge of undulating swimmers, we will use fa' to scale the net thrust. The power, however, was found to scale better with fa. We thus introduce the phase-averaged thrust and power coefficients

$$\tilde{C}_\tau \equiv \frac{\tilde{\tau}}{\rho sc f^2 a'^2} \quad \text{and} \quad \tilde{C}_\wp \equiv \frac{\tilde{\wp}}{\rho sc f^3 a^3}. \tag{3.4}$$

Figure 10 shows a variety of these coefficients for panels B, C, and D. The collapse of the data demonstrates the effectiveness of this scaling approach. The main trends are the same for all cases. As before, two peaks occur per cycle, each at or slightly after

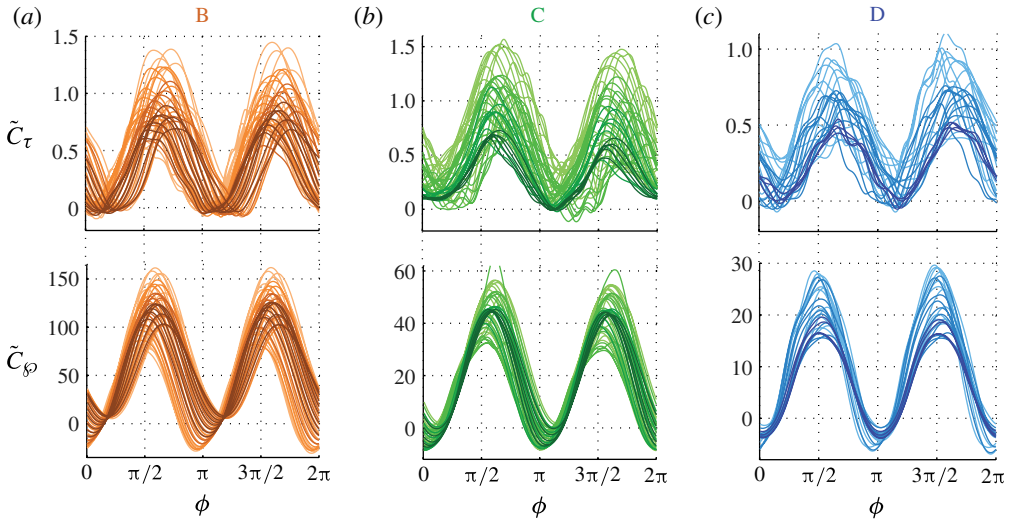

FIGURE 10. (Colour online) Coefficients of net thrust and power: (*a*) panel B, (*b*) panel C, (*c*) panel D. Solid lines show the phase-averaged net thrust and power coefficients through the flapping cycle. The data cover all flow speeds considered. Due to high relative uncertainties at low frequencies, only frequencies leading to positive net thrust ($\bar{\tau} > 0$) are plotted.

the mid-upstroke or mid-downstroke. The scaling did not apply well to the stiffest panel, panel A (results not shown), where the highest $\tilde{C}_\tau$ peaks were roughly four times higher than the lowest peaks, and the phase of the peaks occurred over a range between $\pi/2$ and π. This is not surprising in that there are no bending forces in the proposed scaling. Presumably the bending forces play a larger role in the stiffer panels, and the magnitude and phase of the forces are no longer linked to fluid forces alone.

Exceptions aside, the curves show a comparatively strong collapse, given that before the scaling they differed by as much as two orders of magnitude. Most of the remaining differences result from the flow speed effects mentioned above, where in general higher flow speeds lead to lower values of $\tilde{C}_\tau$. In addition, the peaks occur at similar phases for panels B, C, and D, despite their vastly different kinematics. This observation is consistent with the behaviour of the flow fields, where in many cases the vorticity along the panel was locked in phase with the actuation frequency. It is apparent that the leading edge plays an important role in thrust production, but the exact magnitude of the net thrust depends strongly on the trailing edge amplitude. The fact that the $\tilde{C}_\tau$ peaks are $O(1)$ suggests that the typical thrust forces are relatively unaffected by the bending stiffness. The magnitude of $\tilde{C}_\wp$, however, varies significantly and is not $O(1)$. Without accounting for bending forces, the characteristic power $\rho s c f^3 a^3$ will likely be an underestimate, which helps to explain why $\tilde{C}_\wp \gg 1$, and why it increases with panel stiffness.

3.4. *Time-averaged forces*

Time-averages of the net thrust ($\bar{\tau}$) give insight into the bulk propulsive performance of the panels (figure 11). In general, $\bar{\tau}$ increases with heaving frequency, but does so at different rates, and in some ranges even decreases with frequency. The resulting plateaus are directly related to resonance at the trailing edge. Since the more flexible panels pass through multiple resonant frequencies, they exhibit multiple plateaus. As

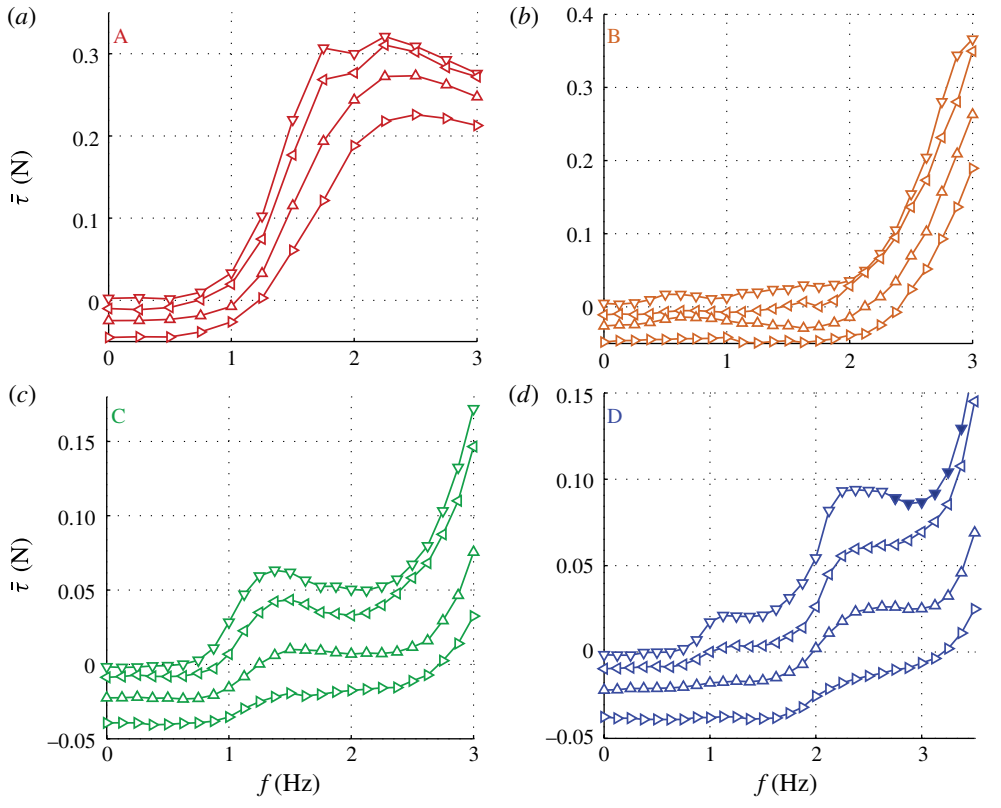

FIGURE 11. (Colour online) Time-averaged net thrust: (*a*) panel A, (*b*) panel B, (*c*) panel C, (*d*) panel D. Symbols as in figure 4.

with the phase-averaged net thrust, higher flow speeds reduce $\bar{\tau}$ in two main ways. One way is by shifting the curves downward, a trend best understood by looking at the static case ($f = 0$ Hz), where viscous drag produces an offset between the net thrust curves. At higher frequencies, the curves differ by more than just an offset, especially with the more flexible panels. This trend suggests that variations beyond the simple offset are due to the different kinematics brought on by higher flow speeds. These two trends can be thought of as being analogous to the two trends in $\tilde{C}_\tau$ mentioned in § 3.3.

To understand the origins of the plateaus, we consider the Lighthill (1970) model for undulating slender fish. For the analysis, it will be useful to scale the time-averaged net thrust with a reference force that is independent of frequency. We therefore use the usual net thrust coefficient based on dynamic pressure:

$$C'_\tau \equiv \frac{\tau}{\frac{1}{2}\rho u_\infty^2 sc}. \tag{3.5}$$

Reformulated using the current notation, the Lighthill (1970) model predicts that

$$\bar{C}'_\tau = \pi\left(\frac{s}{c}\right)\left[St^2\overline{\left(\frac{\partial H^*}{\partial T^*}\right)^2} - \left(\frac{a'}{c}\right)^2\overline{\left(\frac{\partial H^*}{\partial X^*}\right)^2}\right], \tag{3.6}$$

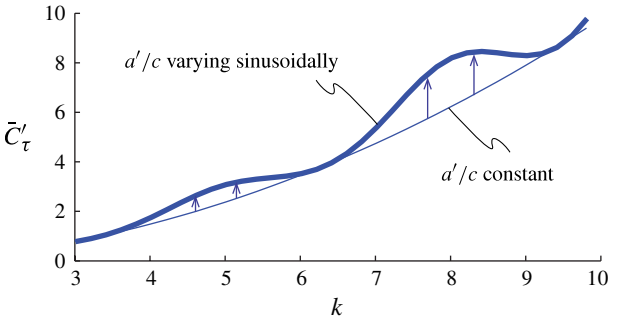

FIGURE 12. (Colour online) Predictions of the Lighthill model for a sinusoidal propulsor. Thin line, $a'/c = 0.1$; thick line, $a'/c = 0.1(1 + 0.15\sin^2 k)$.

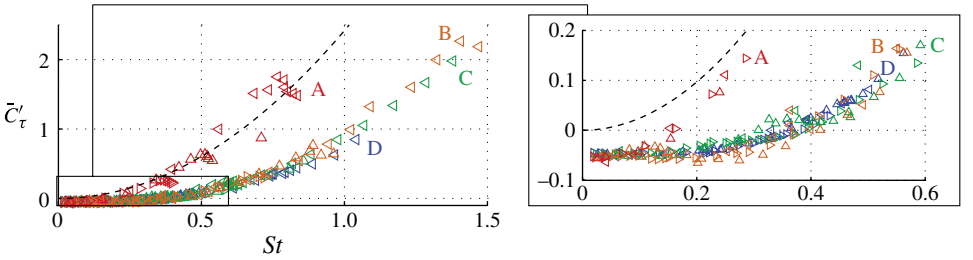

FIGURE 13. (Colour online) Time-averaged net thrust coefficient. The inset shows a magnified view near the origin. Dashed line, $\bar{C}'_\tau = (\pi s/c)St^2$. Symbols as in figure 4.

where the expression is to be evaluated at the trailing edge where $X^* = 1$. Note that this dependence on trailing edge motions alone is consistent with the experiments on anguilliform (eel-like) motion by Hultmark *et al.* (2007), and with the scaling in (3.4). For illustration, consider a panel experiencing a sinusoidal travelling wave with a wavelength equal to the chord, that is, $H^* = 0.5\sin(2\pi(X^* + T^*))$. Figure 12 plots the predicted variation of $\bar{C}'_\tau$ with frequency for the case where a'/c is constant, and where a'/c varies sinusoidally with the reduced frequency ($k \equiv fc/u_\infty$). The local maxima in a' increase the net thrust coefficient such that plateaus appear in the k–$\bar{C}'_\tau$ curve.

Motivated by the coefficients of (3.6), we now plot all the data in the St–$\bar{C}'_\tau$ plane (figure 13). Under the new scaling, plateaus are no longer visible. Specifically, within the plateaus the frequency increases but a' decreases, and the net result is a constant Strouhal number. The plateaus are thus reduced to clusters in St–$\bar{C}'_\tau$ space.

If the panel were perfectly rigid ($EI \to \infty$), H^* would have no spatial variation, and (3.6) then suggests that $\bar{C}'_\tau$ would scale with St^2. This result agrees with the Theodorsen (1935) model for heaving rigid aerofoils and is plotted as a reference in figure 13. As one would expect, this scaling applies best to the most rigid panel (A), except at low Strouhal numbers where the inviscid model neglects the viscous drag present in the experiment. For finite rigidities, H^* varies with X^*, and (3.6) predicts a reduction in $\bar{C}'_\tau$, which is consistent with the data in figure 13. The H^* variation increases at higher structural modes, which are increasingly difficult to actuate at higher frequencies. In other words, a higher jump in frequency is required to move

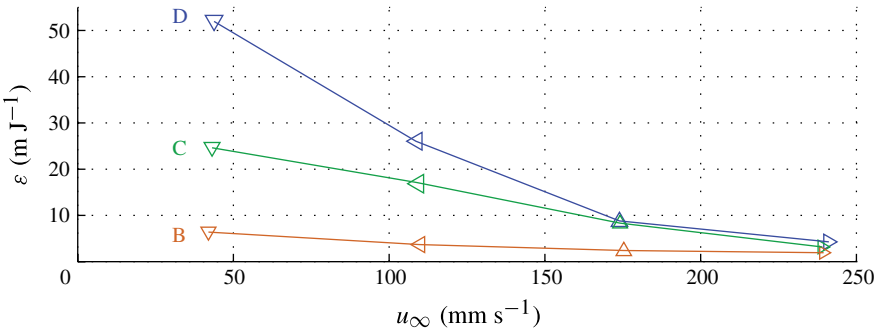

FIGURE 14. (Colour online) Swimming economy. Symbols as in figure 4.

from the second to the third mode than is required to move from the first to the second mode (see figure 3). The result is that the reduction in $\bar{C}'_\tau$ due to variation in H^* is similar over a range of conditions, and within this range of conditions $\bar{C}'_\tau$ is primarily a function of St. This effect is revealed experimentally by the collapse of the $\bar{C}'_\tau$–St curves for panels B, C, and D.

The collapse to a single St–$\bar{C}'_\tau$ curve has significant implications for self-propelled swimming, that is, where the mean net thrust is zero ($\bar{\tau} = 0$). In figure 3, this condition occurs where $\bar{C}'_\tau$ crosses the St axis. If panels B, C, or D were self-propelling at any of the four flow speeds considered, they would necessarily be operating at Strouhal numbers between 0.3 and 0.4. The classic explanation for the tight band of Strouhal numbers observed in fish propulsion is that wake structures are most efficient when $St \approx 0.25 \rightarrow 0.35$ (Triantafyllou, Triantafyllou & Grosenbaugh 1993). Panels B, C, and D, however, can only self-propel at $St \approx 0.3 \rightarrow 0.4$, regardless of the energy it takes to do so. In fact, the swimming economy, $\varepsilon \equiv u_\infty / \bar{\wp}$, at the self-propelled swimming conditions varies by an order of magnitude (figure 14), despite the nearly constant Strouhal number. It appears that the more relevant parameters here are flexibility and flow speed, where ε increases with flexibility and decreases with swimming speed.

We now consider the efficiency. Efficiency can be quantified for thrust-producing conditions ($\bar{\tau} > 0$) by introducing the propulsive efficiency $\eta \equiv \bar{\tau} u_\infty / \bar{\wp}$, which represents the fraction of the power input that results in streamwise kinetic energy gains for the propulsor. It is only defined in positive net thrust conditions and is relevant when a propulsor is accelerating or overcoming the drag on a body to which it is attached. Following Dewey *et al.* (2013), we note that the scaling in (3.4) suggests that $\hat{\eta} \equiv \eta St$ may be a more useful parameter than η itself. Figure 15 shows $\hat{\eta}$ over the full parameter space. Peaks in efficiency occur at or just above the Π_1 values where the trailing edge amplitude was maximal. As with the swimming economy, the efficiency is highest at low flow speeds and high flexibilities. Presumably, the flow separation observed at high flow speeds (figure 7) results in significantly higher drag and lower efficiency. The only exception to this pattern occurs for the conditions with chaotic kinematics, where efficiency experiences a sudden decrease. This only occurred for panel D at the lowest flow speed and at the highest frequencies ($f \geqslant 2.75$ Hz).

The reduction in efficiency at higher flow speeds is more severe for the more flexible panels. For panel D, the reduction is sufficient for the stiffest panel (panel A) to be more efficient than panel D at $u_\infty = 240$ mm s^{-1}. It appears that an efficient

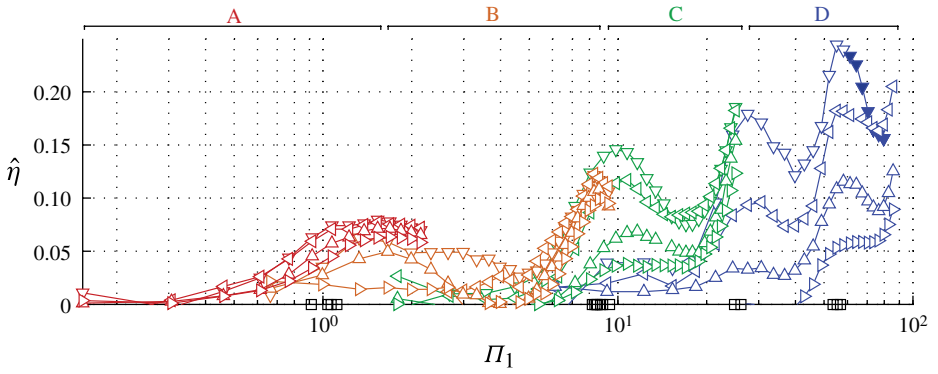

FIGURE 15. (Colour online) Scaled propulsive efficiency. Semi-log scale. Symbols as in figure 4. For reference, locations of a'/a peaks are highlighted along the Π_1 axes (□).

heaving propulsor should swim slowly and be as flexible as possible. If higher speeds are required, a more rigid panel may be more efficient. If the propulsor can adjust its stiffness, it could increase EI when u_∞ is high in order to maximize its efficiency over a range of swimming speeds.

4. Conclusions

Kinematic analysis and direct force measurements have shown that the propulsive performance of heaving flexible panels depends strongly on structural resonance. Trailing edge amplitude is maximized at discrete values of the dimensionless variable Π_1 $(\equiv (\rho s f^2 c^5/EI)^{1/2})$, corresponding to higher levels of net thrust and increased propulsive efficiency $(\equiv \bar{\tau} u_\infty/\bar{\wp})$. This finding is consistent with the results of Alben *et al.* (2012), who numerically discovered multiple local maxima in the self-propelled swimming speeds of heaving propulsors.

Phase-averaged force measurements revealed that net thrust and power experience two peaks during the flapping cycle. For panels B, C, and D, these peaks occur near $\phi \approx \pi/2$ and $\phi \approx 3\pi/2$, regardless of the kinematics along the panel. This suggests that the leading edge plays an important role in thrust production. Particle image velocimetry supported this finding by revealing strong vortices that remained attached to the leading edge throughout the cycle. While thrust production was dominated by the motion of the leading edge, it experienced localized increases when the trailing edge amplitude was maximized. These increases resulted in frequency plateaus in the net thrust curves, an effect that was qualitatively recreated by sinusoidally varying the trailing edge amplitude input into the Lighthill (1970) model.

Higher flow speeds led to lower structural modes present on the panel, separation along the surface of the panel, lower trailing edge amplitude, and lower propulsive efficiencies. The fact that flow separation was correlated with lower efficiencies brings the current study in line with the work of Hultmark *et al.* (2007), who adopt an anguilliform body motion characterized by a travelling wave with an exponentially growing amplitude with distance along the body. As in their study, the results here suggest that thrust increases with trailing edge amplitude, but that efficiency decreases when deflections are sufficient for flow to separate along the surface of the panel. Unlike efficiency, the frequencies at which trailing edge resonance occur were relatively unaffected by flow speed. Furthermore, these resonant frequencies

appeared to align with the frequencies of the eigenmodes for the theoretical case where $u_\infty = 0$ and added mass forces are the only external forces. This result has important implications for propulsor design. A flexible propulsor is able to maintain high efficiency over a range of swimming speeds by operating at certain Π_1 values.

It was shown analytically that when only added mass forces are present, Π_1 is directly proportional to the ratio between the actuation and resonant frequencies, $f/\hat{f}_i$. This helps to relate the current results to the work of Dewey *et al.* (2013), who estimated the first resonant frequency empirically and found that $f/\hat{f}_1$ could be used to collapse their data. Dewey *et al.* (2013) successfully applied scalings based on the Euler–Bernoulli beam equation to pitching motions at one flow speed, where the first resonant frequency was reached. By examining heaving motions, multiple flow speeds, and four resonant frequencies, we have shown that these scalings are applicable over a wide range of flexibilities and swimming conditions.

For panels B, C, and D, the traditional net thrust coefficient ($\equiv \bar{\tau}/(\rho s c u_\infty^2/2)$) was shown to be primarily a function of Strouhal number ($\equiv fa'/u_\infty$). A similar result was found numerically by Paulo *et al.* (2011). The implication is that self-propelled swimming for panels B, C, and D is only possible over a tight range of Strouhal number between 0.3 and 0.4. It is worth noting that a variety of swimmers and flyers in nature swim in this range (Taylor, Nudds & Thomas 2003), although the possibility of coincidence cannot be ruled out, especially since for many fish the propulsor is only a small part of the body. Carangiform swimmers, for example, produce thrust primarily with the caudal fin, and other parts of the body may contribute to increased form drag. This higher drag would add an offset to the St–$\bar{C}'_\tau$ curve in figure 13 and lead to a different Strouhal number range for self-propelled swimming.

Nevertheless, our findings suggest that the usual interpretation of Strouhal number as an indicator of efficiency (Triantafyllou *et al.* 1993) is imprecise. It appears that for the simple case of self-propelled heaving flexible panels, Strouhal number is an outcome determined by the geometry and gait of the panel. We find a nearly constant value of the Strouhal number for self-propelled swimming, but significant variation in the swimming economy ($\equiv u_\infty/\bar{\wp}$). The economy is maximized when the flow speed is low and panel flexibility is high. If the panel were designed to be a propulsor, the Strouhal number in the self-propelled state would be approximately constant, and the economy would be dictated by the swimming speed.

Acknowledgements

This work was supported by the Office of Naval Research under MURI grant number N00014-08-1-0642 (Program Director Dr B. Brizzolara), and the National Science Foundation under grant DBI 1062052 (PI L. Fauci) and grant EFRI-0938043 (PI G. Lauder).

REFERENCES

ALBEN, S., WITT, C., BAKER, T. V., ANDERSON, E. & LAUDER, G. V. 2012 Dynamics of freely swimming flexible foils. *Phys. Fluids* **24**, 051901.

ALLEN, J. J. & SMITS, A. J. 2001 Energy harvesting eel. *J. Fluids Struct.* **15**, 629–640.

ANDERSON, J. M., STREITLIEN, K., BARRETT, D. S. & TRIANTAFYLLOU, M. S. 1998 Oscillating foils of high propulsive efficiency. *J. Fluid Mech.* **360**, 41–72.

BHALLA, A. P. S., GRIFFITH, B. E. & PATANKAR, N. A. 2013 A forced damped oscillation framework for undulatory swimming provides new insights into how propulsion arises in active and passive swimming. *PLoS Comput. Biol.* **9** (6), e1003097.

BUCHHOLZ, J. H. J. & SMITS, A. J. 2006 On the evolution of the wake structure produced by a low-aspect-ratio pitching panel. *J. Fluid Mech.* **546**, 433–443.

DANIEL, T. L. & COMBES, S. A. 2002 Flexible wings and fins: bending by inertial or fluid-dynamic force? *Integr. Compar. Biol.* **42**, 1044–1049.

DEWEY, P. A., BOSCHITCH, B. M., MOORED, K. W., STONE, H. A. & SMITS, A. J. 2013 Scaling laws for the thrust production of flexible pitching panels. *J. Fluid Mech.* **732**, 29–46.

HEATHCOTE, S. & GURSUL, I. 2007 Flexible flapping airfoil propulsion at low Reynolds numbers. *AIAA* **45** (5), 1066–1079.

HULTMARK, M., LEFTWICH, M. & SMITS, A. J. 2007 Flowfield measurements in the wake of a robotic lamprey. *Exp. Fluids* **43**, 683–690.

KANG, C. K., AONO, H., BAIK, Y. S., BERNAL, L. P. & SHYY, W. 2013 Fluid dynamics of pitching of plunging flat plate at intermediate Reynolds numbers. *AIAA* **51** (2), 315–329.

KANG, C. K., AONO, H., CESNIK, C. E. S. & SHYY, W. 2011 Effects of flexibility on the aerodynamic performance of flapping wings. *J. Fluid Mech.* **689**, 32–74.

KATZ, J. & WEIHS, D. 1978 Hydrodynamic propulsion by large amplitude oscillation of an airfoil with chordwise flexibility. *J. Fluid Mech.* **88** (3), 485–497.

LAUDER, G. V., LIM, J., SHELTON, R., WITT, C., ANDERSON, E. & TANGORRA, J. L. 2011 Robotic models for studying undulatory locomotion in fishes. *Mar. Technol. Soc. J.* **45** (4), 41–55.

LAUDER, G. V. & MADDEN, P. G. A. 2007 Fish locomotion: kinematics and hydrodynamics of flexible foil-like fins. *Exp. Fluids* **43**, 641–653.

LEFTWICH, M., TYTELL, E. D., COHEN, A. H. & SMITS, A. J. 2012 Wake structures behind a swimming robotic lamprey. *J. Expl Biol.* **215**, 416–425.

LIGHTHILL, M. J. 1970 Aquatic animal propulsion of high hydromechanical efficiency. *J. Fluid Mech.* **44**, 265–301.

LOW, K. H. 2011 Current and future trends of biologically inspired underwater vehicles. *Tech. Rep.*, Nanyang Technical University.

MICHELIN, S. & LLEWELLYN SMITH, S. G. 2009 Resonance and propulsion performance of a heaving flexible wing. *Phys. Fluids* **21**, 071902.

PAULO, J. S., FERREIRA DE SOUSA, A. & ALLEN, J. J. 2011 Thrust efficiency of harmonically oscillating flexible flat plates. *J. Fluid Mech.* **674**, 43–66.

PEDERZANI, J. & HAJ-HARIRI, H. 2006 Analysis of heaving flexible airfoils in viscous flow. *AIAA* **44** (11), 2773–2779.

PREMPRANEERACH, P., HOVER, F. S. & TRIANTAFYLLOU, M. S. 2003 The effect of chordwise flexibility on the thrust and efficiency of a flapping foil. In *Proceedings of the Thirteenth International Symposium on Unmanned Untethered Submersible Technology*.

RAMANANARIVO, S., GODOY-DIANA, R. & THIRIA, B. 2011 Rather than resonance, flapping wing flyers may play on aerodynamics to improve performance. *Proc. Natl Acad. Sci. USA* **108** (15), 5964–5969.

SCIACCHITANO, A., WIENEKE, B. & SCARANO, F. 2013 PIV uncertainty quantification by image matching. *Meas. Sci. Technol.* **24**, 045302.

SPAGNOLIE, S. E., MORET, L., SHELLEY, M. J. & ZHANG, J. 2010 Surprising behaviours in flapping locomotion with passive pitching. *Phys. Fluids* **22**, 041903.

STANISLAS, M., OKAMOTO, K., KAHLER, C. J. & WESTERWEEL, J. 2005 Main results of the second international PIV challenge. *Exp. Fluids* **39**, 170–191.

TAYLOR, G. K., NUDDS, R. L. & THOMAS, A. L. R. 2003 Flying and swimming animals cruise at a Strouhal number tuned for high power efficiency. *Nature* **425**, 707–711.

THEODORSEN, T. 1935 General theory of aerodynamic instability and the mechanism of flutter. *Tech. Rep.*, National Advisory Committee for Aeronautics.

TRIANTAFYLLOU, G. S., TRIANTAFYLLOU, M. S. & GROSENBAUGH, M. A. 1993 Optimal thrust development in oscillating foils with application to fish propulsion. *J. Fluids Struct.* **7**, 205–224.

VANELLA, M., FITZGERALD, T., PREIDIKMAN, S., BALARAS, E. & BALACHANDRAN, B. 2009 Influence of flexibility on the aerodynamic performance of a hovering wing. *J. Expl Biol.* **212**, 95–105.

WEAVER, W., TIMOSHENKO, S. P. & YOUNG, D. H. 1990 *Vibration Problems in Engineering*, 5th edn. Wiley.

WU, T. Y. 1971 Hydrodynamics of swimming propulsion. Part 1. Swimming of a two-dimensional flexible plate at variable forward speeds in an inviscid fluid. *J. Fluid Mech.* **46** (2), 337–355.

ZHU, Q. 2007 Numerical simulation of a flapping foil with chordwise or spanwise flexibility. *AIAA* **45** (10), 2448–2457.